Icarus 223 (2013) 211–221

Contents lists available at SciVerse ScienceDirect

Icarus

journal homepage: www.elsevier.com/locate/icarus

Remote sensing of the energy of auroral electrons in Saturn's atmosphere: Hubble and Cassini spectral observations

J.-C. Gérard [a,*], J. Gustin [a], W.R. Pryor [b], D. Grodent [a], B. Bonfond [a], A. Radioti [a], G.R. Gladstone [c], J.T. Clarke [d], J.D. Nichols [e]

[a] LPAP, Université de Liège, Belgium
[b] Central Arizona College, Coolidge, AZ 85128, USA
[c] Space Science and Engineering Division, SWRI, 6220 Culebra Road, San Antonio, TX 78238, USA
[d] CSP, Boston University, 725 Commonwealth Avenue, Boston, MA 02215, USA
[e] Radio & Space Plasma Physics Group, University of Leicester, University Road, Leicester LE1 7RH, UK

ARTICLE INFO

Article history:
Received 27 April 2012
Revised 20 November 2012
Accepted 20 November 2012
Available online 10 December 2012

Keywords:
Saturn, Magnetosphere
Aurorae
Ultraviolet observations
Spectroscopy

ABSTRACT

Saturn's north ultraviolet aurora has been successfully observed twice between March and May 2011 with the STIS long-slit spectrograph on board the Hubble Space Telescope. Spatially resolved spectra at ~12 Å spectral resolution have been collected at different local times from dawn to dusk to determine the amount of hydrocarbon absorption. For this purpose, the HST telescope slewed across the auroral oval from mid-latitudes up to beyond the limb while collecting spectral data in the timetag mode. Spectral images of the north ultraviolet aurora were obtained within minutes and hours with the UVIS spectrograph on board Cassini. Several daytime sectors and one nightside location were observed and showed signatures of weak absorption by methane present in (or above) the layer of the auroral emission. No absorption from other hydrocarbons (e.g. C_2H_2) has been detected. For the absorbed spectra, the overlying slant CH_4 column varies from 3×10^{15} to 2×10^{16} cm^{-2}, but no clear dependence on local time is identified. A Monte Carlo electron transport model is used to calculate the vertical distribution of the H_2 emission and to relate the observed spectra to the energy of the primary auroral electrons. Assuming electron precipitation with a Maxwellian energy distribution into a standard model atmosphere, we find that the mean energy ranges from less than 3 to ~10 keV. These results are compared with previous determinations of the energy of Saturn's aurora based on ultraviolet spectra and limb images. We conclude that the energies derived from spectral methods are higher that those deduced from the nightside limb images using current atmospheric models. We emphasize the need for more realistic model atmospheres with temperature and hydrocarbon distributions appropriate to high-latitude conditions.

1. Introduction

Saturn's aurora and magnetospheric dynamics are different from both the solar wind driven case of the Earth and the dominance of corotating plasma at Jupiter. Unlike Jupiter or the Earth, the magnetic dipole of Saturn is closely aligned with the planetary spin axis with an offset angle less than 1 degree. The morphological and spectral characteristics of Saturn's aurora were reviewed by Kurth et al. (2009). The original detection of Saturn's FUV aurora was based on spectra collected with the Ultraviolet Spectrometer (UVS) during the Voyager 1 and two flybys of Saturn in 1980. They showed the presence of the HI Lyman-α and H_2 Lyman and Werner bands in the polar regions of both hemispheres. Saturn's aurora appeared in the Voyager data as a narrow circumpolar region (Broadfoot et al., 1981; Sandel and Broadfoot, 1981), probably originating from the distant magnetosphere. Outbursts of Lyman-α emission were intermittently observed with the International Ultraviolet Explorer (IUE) over a decade (Clarke et al., 1981; McGrath and Clarke, 1992). The Faint Object Camera on board the Hubble Space Telescope (HST) provided the first image of the north Saturn aurora, with all images co-added to increase the signal to noise ratio (Gérard et al., 1995). A set of Wide Field Planetary Camera (WFPC2) FUV images (Trauger et al., 1998) with a higher limiting sensitivity (~5 kR) showed more details of the northern auroral arc. The brightness of the emission was quite variable (<5–90 kR), but the morning sector was consistently enhanced in comparison with the afternoon sector. Gérard et al. (2004) and Grodent et al. (2005) analyzed two sets of FUV images of the north and south polar regions obtained with the Space Telescope Imaging Spectrograph (STIS). They found that the morphology and brightness

* Corresponding author. Address: LPAP, Université de Liège, 17, allée du 6 août, B5c, B-4000 Liege, Belgium. Fax: +32 43669711.
E-mail address: jc.gerard@ulg.ac.be (J.-C. Gérard).

0019-1035/$ - see front matter © 2012 Elsevier Inc. All rights reserved.
http://dx.doi.org/10.1016/j.icarus.2012.11.033

distribution of the aurora vary on time scales of hours or less. They also tentatively identified the optical signature of the dayside cusp near local noon and pointed out the occasional presence of a spiral structure of the main oval. The dayside main oval lies between 70° and 80° and is generally brighter and thinner in the morning than in the afternoon sector. The brightness of the main oval ranged from below the STIS threshold at ~1 kR of H_2 emission up to about 75 kR. The total electron precipitated power was found to vary between 20 and 140 GW, that is comparable to the Earth's active aurora but about two orders of magnitude less than on Jupiter (Gérard et al., 2005; Nichols et al., 2010). Based on images from the Ultraviolet Imaging Spectrograph (UVIS) instrument on board Cassini, Grodent et al. (2011) observed that what appears as a continuous oval on low resolution images could actually be formed of small scale structures in the noon and dusk sectors. Furthermore, Radioti et al. (2011) and Badman et al. (2012) identified bifurcations of the main oval followed by an expansion of this oval. By analogy to the Earth, this behavior was attributed to large-scale reconnections on the dayside magnetopause. Saturn's aurora shows large intensity and morphological variations of the main oval in response to changes in the solar wind dynamic pressure (Clarke et al., 2009). Infrared emissions from the ionospheric H_3^+ ion, whose density is significantly enhanced by auroral precipitation, have also been spectroscopically detected (Geballe et al., 1993) and imaged from the ground (Stallard et al., 2007). Badman et al. (2011) analyzed images obtained with the Visual and Infrared Mapping Spectrometer (VIMS) on board Cassini and showed that the average location of the infrared oval is similar to that of the ultraviolet main emission.

The aurora of giant planets potentially exerts a major influence on the thermal structure and the chemistry of the planets' upper atmosphere (Müller-Wodarg et al., 2006; Melin et al., 2007), although meridional heat transfer to mid- and low-latitudes is not fully understood (Smith et al., 2007). Effects on thermal structure are very dependent on the energy of auroral electrons and the altitude of deposition of heat by particle precipitation and Joule heating. Cowley et al. (2008) suggested that the auroral oval at Saturn corresponds to a ring of upward current bounding the region of open and closed magnetic field lines. Their model estimated that the aurora is produced by magnetospheric electrons accelerated to energies in the range of a few keV to a few tens of keV. Coordinated HST-Cassini observations have indicated that field-aligned currents and potential acceleration play a key role in Saturn's aurora (Bunce et al., 2008) and their in situ signatures have been statistically analyzed by Talboys et al. (2011).

Information on the energy of the precipitated auroral electrons has only been obtained through spectroscopic remote sensing. For example, the altitude of the aurora relative to the hydrocarbon homopause has been derived from the comparison between the observed spectra and a reference H_2 laboratory spectrum without any absorption. The methane column providing the best fit allows the determination of the altitude of the auroral emission peak relative to the hydrocarbon homopause, which is linked to the energy of the precipitating electrons. This method is based on the shape of the CH_4 absorption cross sections, which partly absorbs the H_2 emissions at wavelengths less than 1400 Å but leaves the longer wavelength H_2 emissions unattenuated. Low spectral resolution Voyager-UVS spectra provided indications on the nature and energy of the auroral energetic particles interacting with Saturn's atmosphere (Sandel and Broadfoot, 1981; Sandel et al., 1982; Shemansky and Ajello, 1983). Spectra generally appeared to originate near the exobase (near 2500 km) and showed no signature of hydrocarbon absorption, with the exception of the brightest spectrum which was best fitted with an overlying methane column of 8×10^{15} cm^{-2}. The STIS spectrograph on board Hubble offered the possibility to obtain spatially resolved spectra together with images of the auroral emission morphology measured a few minutes before or after the spectra. Six STIS FUV auroral spectra collected in December 2000 with a 12-Å spectral resolution in the noon sector were compared with a synthetic model of electron-excited H_2 emissions. The wavelengths below 1400 Å were weakly absorbed by methane with column densities ranging between 7×10^{15} and 2×10^{16} cm^{-2}. These results suggested that the aurora is emitted near the homopause, located at ~800 km in the model atmosphere developed by Moses et al. (2000) based on low-latitude Voyager solar occultation. The mean energy of the primary auroral electrons was estimated in the range 12 ± 3 keV. A comparison of FUV spectra observed with STIS-HST on one hand and with the UVIS spectrograph on board Cassini on the other hand was presented by Gustin et al. (2009). They found that the vertical column of CH_4 overlying the principal layer of auroral emissions ranges from 1.4×10^{15} to 1.2×10^{16} cm^{-2}, corresponding to a mean energy of 10–18 keV, using the Moses et al. (2000) model adapted to the value of gravity at 75°N.

Another useful remote sensing technique to estimate the depth of the auroral emission Gustin et al. (2004) is based on absorption of the EUV H_2 bands. Self-absorption was observed with Voyager-UVS in a bright spectrum (~100 kR) (Sandel et al., 1982; Shemansky and Ajello, 1983). High resolution (0.2 Å) EUV spectra collected with the Far Ultraviolet Spectroscopic Explorer (FUSE) satellite showed that the 1090–1180 Å spectrum was not self-absorbed and characterized by a temperature of 400 K at the altitude of the bulk of the auroral EUV emission (Gustin et al., 2009), in agreement with the values obtained from H_3^+ infrared polar spectra (Melin et al., 2007). A FUSE spectrum between 1030 and 1080 Å including transitions connecting to the $v = 0$ or 1 vibrational levels of the electronic ground state was also analyzed by Gustin et al. (2009). It exhibited self-absorption by a H_2 vertical column of 3×10^{19} cm^{-2} above the aurora, which locates the auroral layer near 660 km in the atmospheric model at 75°N. If this H_2 column is used to determine the energy of precipitating electrons, it corresponds to primary electrons of ~10 keV, in good agreement with the STIS results. The total electron energy range of 10–18 keV deduced from the STIS and FUSE observations sets the auroral emission peak close to the 0.1 μbar pressure level, that is slightly above the methane homopause. FUSE spectra could not provide any spatial resolution, so that the temperature and the auroral pressure level refer to global average values integrating emission from all local times and different view angles.

A third, less model dependent, source of information on the energy of the auroral electrons is the altitude of the peak of the H_2 emission observed in FUV images beyond Saturn's high latitude limb. Gérard et al. (2009) analyzed more than 176 radial light curves collected with the Advanced Camera for Surveys (ACS) on board Hubble. They found that the peak of the nightside emission is statistically located at 1145 ± 305 km above the altitude of the 1-bar level. The altitude of the H_3^+ infrared auroral emission was also found to be 1155 ± 25 km, in close agreement with the FUV emission (Stallard et al., 2012). Gérard et al. (2009) suggested that the spectral and the imaging results can only be reconciled if the thermal structure of the high-latitude thermosphere is different from the reference model used for their analysis. They proposed an alternative empirical model meeting the observational constraints for auroral latitudes. In this alternative model, the stratospheric temperature gradient is maximum near 10 μbars, compared to 7×10^{-3} μbar in the standard model. As a consequence, the 0.1 μbar auroral level derived from the FUSE spectrum is located near 1200 km in this model, in agreement with the HST limb images. The characteristic energy of the auroral electrons reaching this level was estimated in the range 1–5 keV using the 75° latitude model adapted from Moses et al. (and 5–30 keV in case of the modified model). These observational results are synthesized in Table 1

that lists the results of the spectral and imaging observations including the present results. To summarize, it appears that a discrepancy exists between the altitude determination based on direct imaging of the ultraviolet auroral emission at the limb and the level derived from ultraviolet spectroscopy, unless the thermal structure of the high latitude atmosphere is markedly different from that derived from the adopted model atmosphere. Further observations are needed to extend the very limited database currently available and determine the absorption by hydrocarbons in the aurora at different local times.

HST measurements of Saturn's FUV spectrum have been obtained recently to address this question by combining FUV auroral images and spatially resolved spectroscopy. Some of these HST observations made in 2011 were coordinated with quasi-simultaneous observations of the north aurora with the UVIS spectrograph on board Cassini. In particular, we took advantage of the spatial resolution of STIS and UVIS to isolate specific regions of the aurora other than the noon sector, and extend the analysis to nightside conditions. The observations are described in Section 2 and two different approaches to analyze the spectra are described in Section 3. Section 4 presents estimates of the overlying column of methane and simulations of the auroral electron penetration in Saturn's upper atmosphere based on a Monte Carlo electron transport code. The results of the comparison of the model simulations with the spectral observations are discussed in Section 5 and compared with earlier determinations of the altitude of the aurora and the characteristic energy of the primary electrons.

2. Observations

2.1. The instruments

Observations were made using two instruments on two different spacecraft. One is the STIS FUV-MAMA imaging spectrograph on board HST. It was operated both in the imaging mode to obtain the global auroral context near the time of the spectral observations and in the long-slit spectral mode. The CLEAR mode (no filter) was used for the images to provide the highest possible signal to noise ratio. Its passband roughly extends from 1100 to 2000 Å, therefore including a small Lyman-α contribution. Time-tagged dayside auroral spectra were successfully obtained with the STIS in the G140L mode with the 52×0.5 arc sec aperture, covering the wavelengths 1150–1700 Å at a spectral resolution of $\sim$12 Å. The time-tag mode makes it possible to analyze the photon stream reaching the detector and to isolate space and/or blocks during the post-processing phase. The STIS instrument, its observing modes and on-orbit performance were described by Kimble et al. (1998).

The second one is the FUV channel of the UVIS instrument on board Cassini orbiting Saturn, whose passband is 1115–1912 Å. The detector is a pulse-counting microchannel plate equipped with a CODACON readout anode. Similarly to STIS, the two-dimensional format of the detector allows simultaneous spectral and one-dimensional spatial coverage (Esposito et al., 2004). The UVIS slit image on the detector is covered by 1024 pixels in the dispersion direction and 64 pixels in the spatial direction. Different slit widths are available on the UVIS FUV channel. The spectra analyzed here were collected with the 150-μm slit which provides a providing FWHM spectral resolution of $\sim$5.5 Å on an extended source.

2.2. The observational sequences

On three occasions the Hubble Space Telescope performed slew maneuvers to move the slit projection across the north polar region. In this way, the slit of the STIS instrument scanned the north polar region from southward of the auroral equatorward boundary to beyond the north limb of the planet while continuously collecting FUV spectra of the aurora (Fig. 1i). The slit was inclined at low angle relative to the planetary equator to optimize the use of the long slit and maximize the chances to intercept the strongest emission regions during the telescope slew. The observations were divided into 3 visits of 2 orbits each, which took place on March 17, April 17 and May 10, 2011. The aurora was too weak on May 10 and the signal to noise ratio of the spectra too low to provide useful data. Similarly, the higher resolution spectra (G140M mode) collected during the second orbit of the three visits were too noisy and will not be discussed here. The start times and exposure lengths of the first two HST visits and the associated UVIS observations are listed in Tables 2 and 3. The calibration of the STIS spectra follows the procedure described in Gustin et al. (2009). Changes in the sensitivity of the instrument during the mission, including the relative response of different wavelengths, are taken into account by monitoring bright hot star spectra.

2.2.1. March 17, 2011

Fig. 1i shows the FUV STIS image obtained during the first visit in the CLEAR timetag mode, a few minutes before the STIS spectra, in order to visualize the global morphological context. The main north auroral oval is clearly observed on the dayside with the highest brightness level observed in the early morning sector. A nightside ring of emission is also present near the polar limb although it is significantly weaker. The intensity of the total H_2 emission in the 700–1800 Å window is estimated to reach 30 kR in the bright region located in the morning sector. We used the conversion factors from counts/s pixel to kR determined by Gustin et al. (2012). The

Table 1
Summary of observations available to determine the level of Saturn's ultraviolet aurora.

Observations	Vertical CH_4 column (10^{15} cm^{-2})	Vertical H_2 column (10^{19} cm^{-2})	Peak pressure (μbar)	Peak altitude (km)	Mean electron energy (keV)
HST/STIS	**4.2–12**	5.0–8.2	0.2–0.3	610–630	13–18
Cassini UVIS FUV (Gustin et al., 2009)	**1.4**	3.1	0.1	655	10
FUSE Lif1a (Gustin et al., 2009)	–	**3.0**	0.1	655	10
FUSE Lif2a (Gustin et al., 2009)	–	⩽**6.0**	⩽0.2	⩽625	⩽15
HST/ACS (Gérard et al., 2009)	–			**800–1200**	0.3–2
This work	**no abs – 5.7**	⩽5.7	⩽0.2	⩽625	⩽21

Bold characters: measured values; standard characters: values derived using a model atmosphere.
STIS and UVIS spectra: pressure, altitudes, and vertical H_2 columns were derived from the Moses et al. (2000) atmospheric model adapted to 75° latitude. The electron energies determined in previous studies are derived from a stopping power table. They are determined from Monte Carlo simulations in the present study.
FUSE spectra: the pressure levels are determined assuming hydrostatic equilibrium and the electron energies were directly derived from a stopping power, without the need of an atmospheric model.
ACS images: Moses et al.'s (2000) model at 75° was used to convert the observed altitudes into H_2 column, and the corresponding electron mean energy was determined from Monte Carlo simulations for monoenergetic beams.

Table 2
STIS images obtained during the 2011 HST-Cassini UV spectral campaign.

Date	UT	HST File ID	Exposure (s)	Detector	Filter
17 March	18:06	obhu32twq	395	MAMA	CLEAR
17 April	21:44	obhu21btq	345	MAMA	CLEAR

Table 3
STIS G140L and UVIS observations during the 2011 HST-Cassini UV spectral campaign.

Date	UT	Instrument	Spectrum label	Exposure (s)	Mean emission angle (°)
17 March	18:26	STIS	a	1440	75
17 March	19:49	UVIS	b	10080	78
17 March	19:49	UVIS	c	10080	78
17 April	22:03	STIS	d	1500	69
17 April	22:03	STIS	e	1500	85
17 April	19:44	UVIS	f	16200	78
17 April	19:44	UVIS	g	16200	78
17 April	19:44	UVIS	h	16200	78
17 April	19:44	UVIS	i	16200	78
17 April	19:44	UVIS	j	16200	78

geometry of the Saturn view from Earth orbit during the HST observations is shown in Fig. 1ii. The red-colored segment labeled a corresponds to the morning section of the aurora used to construct the STIS spectrum. It extends from the dawn terminator to close to 1200 LT. Immediately following this exposure, a 24-min spatially resolved STIS spectrum was acquired. During this period, the telescope slewed from south to north across the north aurora as illustrated by the projection of the STIS slit position in Fig. 1i.

UVIS observations from Cassini started approximately 1.4 h after the STIS spectrum. They were made from equatorial orbit at a distance of ~27 Saturn radii (R_S), in the vicinity of the 10 PM local time meridian, with the UVIS slit perpendicular to Saturn's equatorial plane. The field of view along the slit was 64 mrad, corresponding to 3227 km projected on Saturn from a distance of 1 R_S. The observations were binned on board over two pixels along the wavelength axis, corresponding to a 1.5 Å width, while the spatial direction was not rebinned. Fig. 1iii presents the composite ultraviolet image generated over a 2 h and 48 min period of observations. The spectral data were grouped into two sets corresponding to the red-colored b and c auroral zones. The location of these two regions is indicated in Fig. 1iv representing the geometry of the UVIS observations from the Cassini spacecraft standpoint. They correspond to the dusk meridian and the early night sectors respectively.

2.2.2. April 17, 2011

During the second visit, on April 17, 2011 the HST STIS slit was inclined by about 25° on the Kronian equator during the south-north telescope slew. as seen in Fig. 2i. An image of the north aurora was collected during the first 345 s, followed by a 1500-s time-tagged G140L spectrum obtained during a telescope slew of the north polar region. The image shows an enhanced region of emission in the pre-noon sector and a secondary bright region in the afternoon sector. A maximum intensity of 28 kR of total H_2 emission was observed near 11:00 LT. The slit projection then slewed from south to north across the aurora to the extent illustrated in Fig. 2i. The auroral intensity was high enough to spatially integrate the STIS spectra over the two different regions of the oval shown in

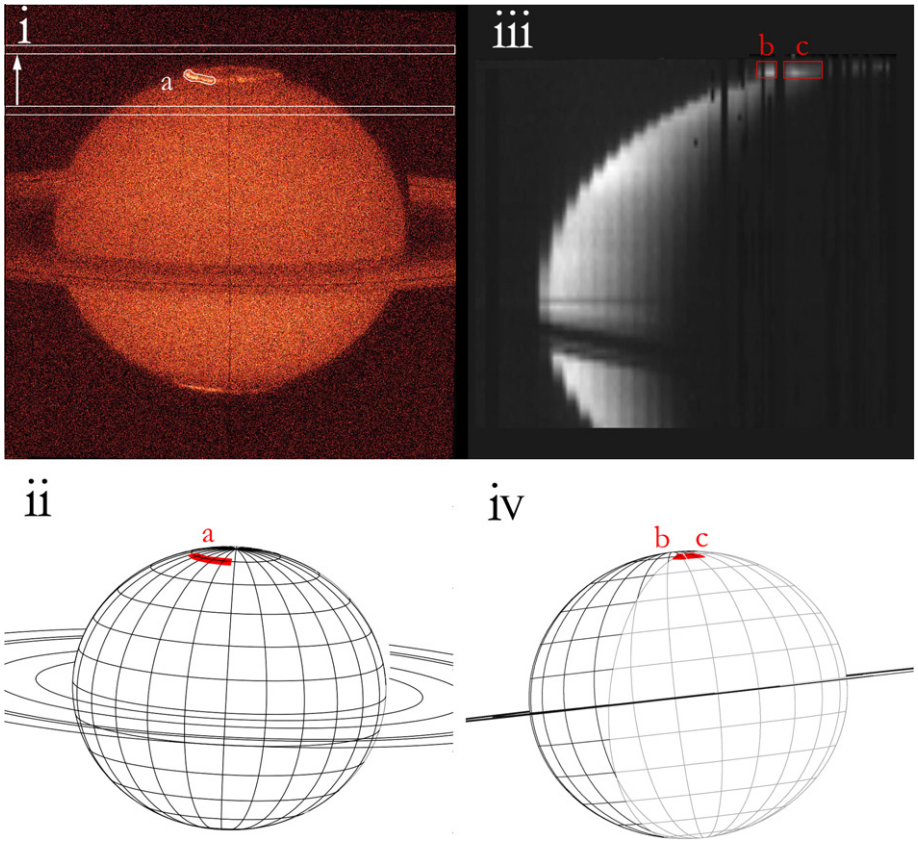

Fig. 1. Geometry of the STIS and UVIS observations on March 17, 2011. i: STIS MAMA image of Saturn' aurora obtained during HST visit 1. The STIS width and the extreme positions of the STIS slit during the telescope slew are shown by the white rectangles. ii: viewing geometry of the observations during the STIS spectral observations; iii: reconstructed image collected by UVIS; iv: viewing geometry during the UVIS observations. The red auroral segments indicate the auroral regions included to build up the three STIS and UVIS spectra shown in Figs. 3 and 4.

Fig. 2i and ii and still get sufficient signal. Zone d extends from the dawn ansa to near local noon while the second (zone e) covers the afternoon and evening sectors.

The UVIS spectral images of the north auroral region were obtained between 20:12 and 23:02 UT, encompassing the time period of the STIS spectral observations. The spacecraft distance from Saturn was ~7.5 R_s, close to the 11:00 LT meridian, so that observations were essentially made on the dayside. Fig. 2iv shows the Saturn disk viewed from the Cassini standpoint and illustrates the geometry of the UVIS observations. In this case, the slit was parallel to the planetary equator. The Cassini spacecraft was successively oriented so that the slit projection on the planet was moved to five different locations from the dawn to the dusk meridians to fully cover the north auroral oval.

The successive positions during which the UVIS slit spatially scanned the region from the dawn limb to the dusk are represented in Fig. 2iii and iv by five red-colored zones labeled f, g, h, i and j In this way, the dayside north auroral region was sequentially observed over the 4.5 h of UVIS observations. The spectral and spatial resolutions were identical to those of visit 1.

3. Methodology of the spectral analysis

To analyze the STIS and UVIS spectra we use two different approaches. The first one (referred to as two layer model in Section 4) is based on a simplified approach where one assumes that a partly absorbing methane layer overlies the auroral source region of H_2 and Ly-α emissions. An unabsorbed laboratory spectrum excited by bombardment with 100-eV electrons (Dziczek et al., 2000) obtained at very low H_2 pressure (about 0.01 bar) under optically thin conditions is used to simulate the auroral source. The amount of CH_4 molecules in the overlying region is obtained when the attenuated spectrum best fits the observed HST or STIS spectrum. This procedure was described and applied to Saturn's aurora by Gérard et al. (2004) and Gustin et al. (2009). The methane column providing the best agreement with the observed spectrum is determined by varying this column and minimizing the chi-squared residual. The methane absorption cross sections measured by Kameta et al. (2002) from 520 to 1220 Å and by Lee et al. (2001) from 1220 to 1520 Å have been adopted here.

The second method corresponds to a more realistic description of the physical processes where the emitting and absorbing regions overlap over a wide range of altitudes. It is based on the use of the numerical model used to calculate electron transport in H_2-dominated atmospheres. It was shortly described by Gérard et al. (2009) and Bonfond et al. (2009) who applied it to the determination of the altitude of Saturn's FUV aurora and of Io's footprint and tail. More details on the numerical method were given by Shematovich et al. (1994). In summary, the energetic electrons interact with the ambient neutrals and lose their excess kinetic energy in elastic, inelastic and ionizing collisions with the H_2 molecules, H and He atoms in the ambient atmospheric gas. Secondary electrons are created following ionizing collisions and are randomly assigned an isotropically distributed pitch angle and an energy following the

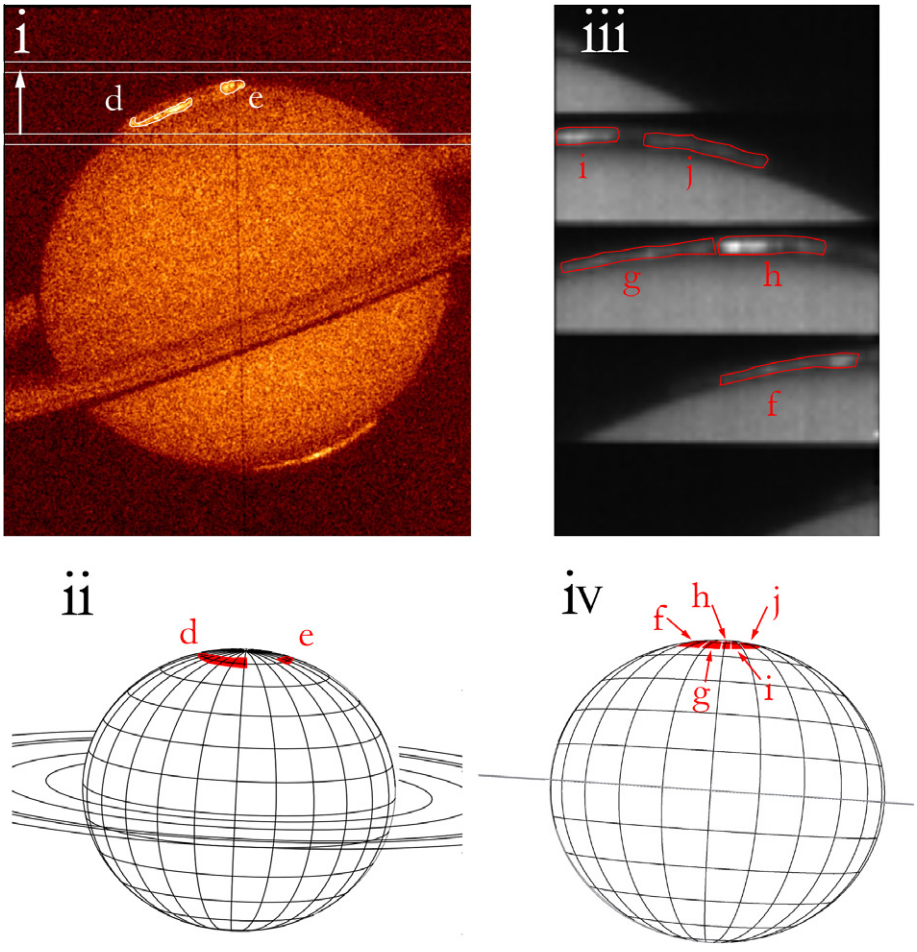

Fig. 2. Geometry of the STIS and UVIS observations on April 17, 2011. i: STIS image of Saturn' aurora obtained during HST visit 2. The STIS width and the extreme positions of the STIS slit during the telescope slew are shown by the white rectangles. ii: viewing geometry of the STIS observations; iii: reconstructed image of the auroral zone collected by UVIS (see text); iv: viewing geometry during the UVIS observations. The red auroral segments marked in ii and iv indicate the emission regions included to build up respectively the two STIS spectra shown in Figs. 3 and 4 and the five STIS spectra.

procedure given by Garvey and Green (1976), Jackman et al. (1977) and Garvey et al. (1977). The electron transport is described by the Boltzmann kinetic equation. The Direct Simulation Monte Carlo (DSMC) method is used to solve atmospheric kinetic systems in the stochastic approximation. The cross sections and scattering angles to calculate the energy loss associated with elastic and inelastic collisions of electrons are taken from the AMDIS database (https://dbshino.nfs.ac.jp) and Shyn and Sharp (1981) for H_2; from the NIST database (http://physics.nist.gov/PhysRefData/Ionization/) and Jackman et al. (1977) and Dalgarno et al. (1999) for helium and atomic hydrogen. The lower boundary is set to an altitude of one bar and the upper boundary is fixed at 1.6×10^{-12} bar where the atmospheric gas flow is practically collisionless. Between these two boundaries, the atmosphere is divided into 49 vertical cells uniformly distributed on a logarithmic pressure scale. In the simulations, we assume that the electrons are isotropically distributed over the lower hemisphere at the upper boundary of the model. The evolution of the system of modeled particles due to collisional processes and particle transport is calculated from the initial to the steady state. As was done previously, the neutral model atmosphere by Moses et al. (2000) is adopted, modified for a gravity acceleration of 11.96 m s^{-2} at the one bar level, prevailing at 75°N. The vertical distribution of methane was calculated using a steady state diffusion model. The molecular and eddy diffusion coefficients, including their pressure dependence, are taken from Moses et al. (2000). The methane mixing ratio from their model in the homosphere is adopted as the lower boundary condition also located below the homopause.

The model provides the emission rate profile for the H_2 Lyman and Werner bands. It calculates the volume emission rates P(z) of the B and C states for an incident electron flux with a prescribed energy distribution. The emergent intensity per unit interval I_λ at wavelength λ is given by:

$$I_\lambda = \int P_\lambda(z) e^{-\tau_\lambda} ds \quad (1)$$

where $P_\lambda(z)$ is the total volume emission rate of the H_2 B → X and C → X transitions at wavelength λ and altitude z and the slant integral (represented by coordinate s) extends along the line of sight from the bottom of the auroral emission layer up to the top of the model. The optical depth at wavelength λ overlying altitude z is denoted $\tau_\lambda(z)$ and is given by:

$$\tau_\lambda(z) = \sigma_\lambda(CH_4) \int_z^\infty n_{CH_4} ds \quad (2)$$

where $\sigma_\lambda(CH_4)$ is the methane absorption cross section at wavelength λ and n_{CH_4} the local number density of methane. The path length ds corresponds to the thickness of a layer multiplied by the Chapman function Ch(χ), where χ is the mean emission angle. In this study, we use the vertical distribution of methane from the low-latitude model by Moses et al. (2000) adapted to 75°N. Since the Monte Carlo model calculates $P_\lambda(z)$ in 49 discrete cells, integration (1) is performed numerically. The attenuation matrix $exp(-\tau_\lambda(z))$ is also calculated for the 49 altitude values and a discrete number of wavelength intervals corresponding to the sampling of interval of the STIS or UVIS spectra. The energy distribution of the precipitating electrons can be prescribed by the user. A Maxwellian energy law was applied in the following simulations. We now describe the results obtained with the two methods.

4. Spectral results

4.1. Two-layer model

Fig. 3a shows the G140L spectrum collected on March 17 in the time-tag mode while the slit scanned the high-latitude Saturn disk. The spectrum (black solid line) was obtained by adding all photon events collected along the main auroral oval. For comparison, the unabsorbed H_2 laboratory spectrum by Dziczek et al. (2000) is also shown as a dotted blue line. It has been smoothed at the same spectral resolution as the STIS spectrum. The agreement is excellent beyond 1300 Å but, at shorter wavelengths, the STIS spectrum significantly departs from the unattenuated laboratory spectrum as a consequence of absorption by methane. In the case of this global STIS spectrum, the best agreement is obtained when the auroral emission is attenuated by an overlying slant methane column of 1.9×10^{16} cm^{-2}. If one assumes that the observed intensity varies as secant of the emission angle, this value corresponds to a vertical column of 4.9×10^{15} cm^{-2}. It should be noted that we use a mean emission angle for each spectrum, as the spectra are extracted from extended regions covering substantial latitude and longitude ranges. The UVIS spectra shown in Fig. 3b and c correspond to regions labeled b and c in Fig. 1iii and iv. The first one only shows minor differences between the laboratory and the observed spectrum, while the second one, obtained on the nightside, is partly absorbed below 1280 Å. The best fit for this second spectrum is obtained for overlying slant CH_4 column of 2×10^{16} cm^{-2}, providing a slightly better fit than a zero column and corresponding to a vertical column of 4.2×10^{15} cm^{-2}. A significant difference is thus observed between the dayside STIS and UVIS spectra on one hand, and the nightside UVIS spectrum on the other hand. These results and those of the other visit are summarized in Table 4. The calibration accuracy of the STIS and UVIS instruments are known within an uncertainty of ~15%. Hence, errors on the column densities retrieved by our fitting procedure are estimated to be also ~15%.

Fig. 3d and e shows the two STIS spectra collected during the telescope slew, on April 17 in the afternoon and the morning auroral regions respectively. They both show departures from the unattenuated laboratory spectrum at short wavelength associated with the signatures of methane absorption. The slant CH_4 columns are 1.2×10^{16} and 1.5×10^{16} cm^{-2} respectively, corresponding to vertical values of 1.1×10^{15} and 5.7×10^{15} cm^{-2}.

As mentioned in Section 2.2.2, the Cassini spacecraft was successively oriented so that the projection of the UVIS slit on the planet was moved to five different locations from the dawn to the dusk meridians to fully cover the north auroral oval. For each successive location, the slit projection slewed from north to south across the aurora to the extent illustrated in Fig. 2iii. The data were grouped into a set of five spectra shown in Fig. 3f–j covering the auroral zone from dawn to dusk. The two (f and g) spectra from the morning side were best fitted with methane slant column densities of 8.8×10^{15} and 1.0×10^{16} cm^{-2}. No absorption was seen in the noon sector, which sets an upper limit on the order of $\sim 5 \times 10^{15}$ cm^{-2} on the slant column of methane. Similarly, the afternoon and evening sectors did not show any signature of hydrocarbon absorption.

The second (multi-layer) method involves a detailed consideration of the vertical distribution of the auroral volume emission rate (VER). In the next section, we first describe the electron transport model used to calculate the auroral electron energy loss in Saturn's atmosphere. We then use this multi-layer model to determine the characteristic energy of the precipitated auroral electrons and compare them with those based on the two-layer approach.

4.2. Multi-layer Monte Carlo model

Fig. 4a–j illustrates the comparison between the UVIS and STIS spectra, the unabsorbed laboratory spectrum and the emerging spectra calculated with the second (multi-layer Monte Carlo) method described in Section 3 using the characteristic electron energy best fitting each spectrum. The last column of Table 4 presents a summary of the results of the best fits to the three STIS and the

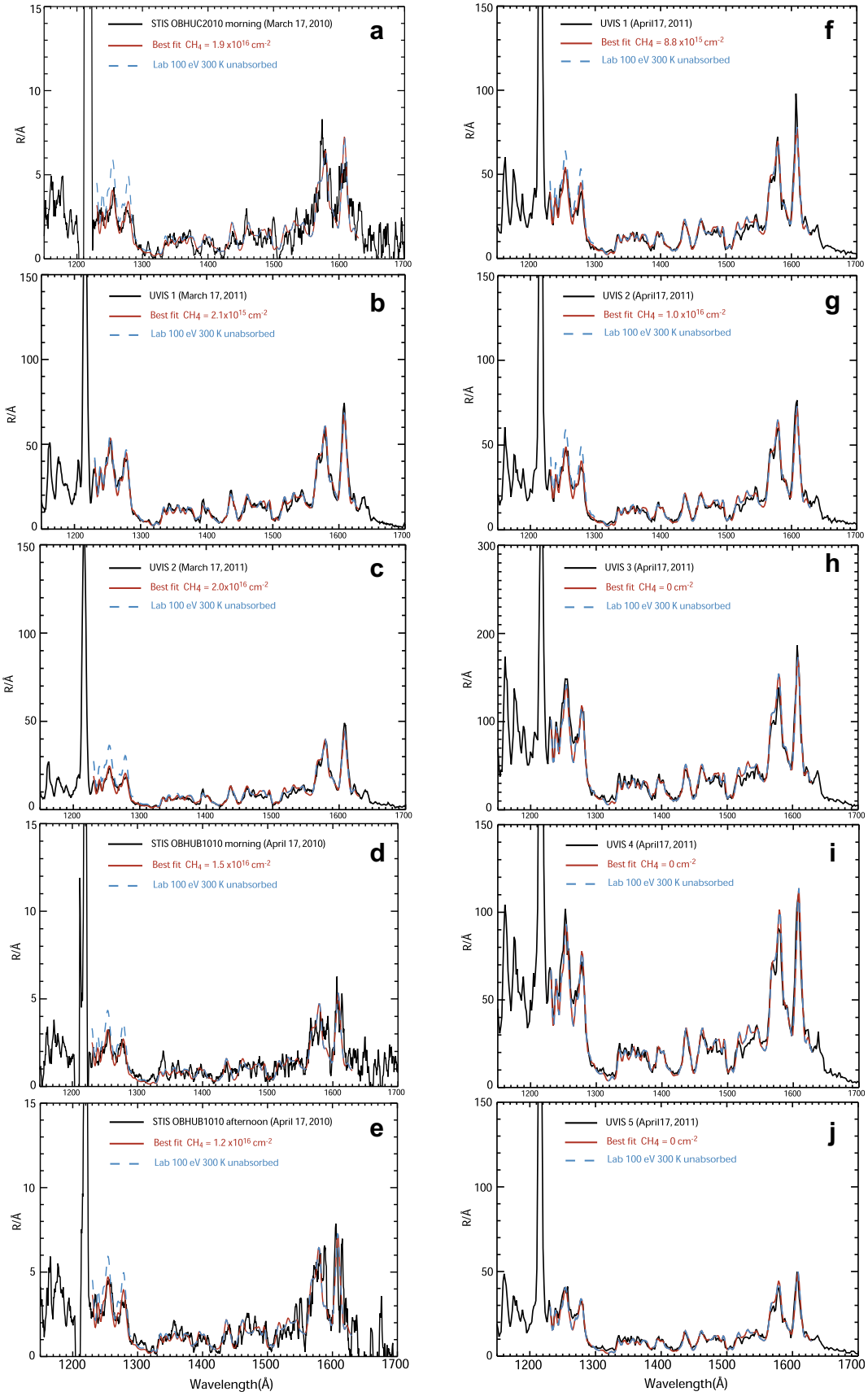

Fig. 3. Auroral spectra obtained on March 17 and April 17, 2011. In each one, the black solid line represents the observations, the blue dotted line the unabsorbed laboratory spectrum and the red solid line the laboratory spectrum attenuated by an overlying layer of methane. The (a–j) labels correspond to the regions marked in Figs. 1 and 2. The conditions of the observations are listed in Table 2. Spectra a, c, d, e, f and g show signatures of absorption by methane below 1280 Å.

Table 4
Methane column and characteristic auroral electron energy derived from the 2011 STIS and UVIS observations.

Spectrum label	Instrument	Date	Mean emission angle (°)	CH_4 slant column (10^{15} cm^{-2})[a]	Energy (keV)[b]
a	STIS	17 March	75	19	10.5
b	UVIS	17 March	78	<5	<3
c	UVIS	17 March	78	20	9.0
d	STIS	17 April	69	15	10.0
e	STIS	17 April	85	12	6.2
f	UVIS	17 April	78	8.8	5.9
g	UVIS	17 April	78	10	6.5
h	UVIS	17 April	78	<5	<3
i	UVIS	17 April	78	<5	<3
j	UVIS	17 April	78	<5	<3

[a] Overlying column of methane, based on the model atmosphere. The error on these values is estimated to ~15% (see text).
[b] Characteristic energy of the Maxwellian electron energy distribution (=half the mean energy).

seven UVIS spectra collected during this campaign. The value listed in the last column is the E_0 characteristic energy in the expression of the Maxwellian energy flux distribution $\Phi(E) = AE\exp(-E/E_0)$, where A is a constant proportional to the energy flux and E_0 is equal to half the mean energy of the distribution. Specifically, the Monte Carlo code was run to generate a series of vertical profiles of the H_2 auroral emission. These profiles were attenuated according to relations (1) and (2) and the predicted emerging spectrum for the specific geometry of each observation was calculated. Based on the values of E_0 bracketing the observed spectrum, additional emission profiles were calculated and corresponding spectra generated until the best fit to the observations was finally obtained. It is estimated that the uncertainty in the determination of E_0 associated with this fitting procedure is about 20%. We first note that the spectra collected with STIS and UVIS give similar values of characteristic energies in spite of the different observation distances to Saturn and viewing geometry. The E_0 values range from less that ~3 keV (no measurable absorption) up to 10.5 keV. As expected, the highest energy value (10.5 keV) is associated with the largest methane column density. Conversely, the lowest E_0 value (5.9 keV) corresponds to the smallest observed CH_4 density. As an illustration of the distribution of the H_2 Lyman and Werner emission profile, Fig. 5 shows the volume emission rate distributions calculated for characteristic energies $E_0 = 1$, 10 and 15 keV. The distribution of the methane density in the model is also indicated, both for the original version of the Moses et al. (2000) model at 30° and for the version adapted to the gravity at 75°N adopted for these calculations. The altitude of the homopause obtained by equaling the molecular and the eddy diffusion coefficients in these models is 870 km at 30° and 730 km at 75°. However, large uncertainties remain in the literature between the various determinations based on different indicators. The possible dependence on latitude of the vigor of turbulent transport near the homopause is also unknown. Energy values reaching ~10 keV were observed with STIS on March 17 in the morning sector, with UVIS in the dusk sector and with STIS on April 27 in the afternoon sector. The UVIS spectra on April 17 indicate a clear difference between the first two spectra (morning) and the last three (noon and afternoon), suggesting that, at this time, the electron precipitation was harder in the morning region than in the afternoon. This difference may indicate that different auroral features were actually observed in the two spectra. However, the March 17 spectra and the STIS spectra of April 17 indicate that this is not a constant pattern. Globally, these observations performed during this campaign clearly demonstrate that the characteristic energy of the auroral electrons at Saturn is variable, probably both in space and in time. The changing pattern of the mean energy does not clearly emerge, possibly because of the limited statistics. It is also possible that the variations of the electron energy are not associated with a specific local time sector, but rather with auroral activity, likely linked to magnetospheric and solar activity conditions.

5. Comparison with earlier results

The six STIS spectra obtained with STIS in December 2000 in the noon sector were analyzed by Gérard et al. (2004) and Gustin et al. (2009) using the first (two-layer) method described in Section 3. All of them showed signatures of absorption by CH_4 with a vertical column in the range 4.2×10^{15}–1.2×10^{16} cm^{-2}, that is a range of values very similar to those reported for the new spectra exhibiting a measurable absorption at short wavelengths. The concept of an emitting layer overlaid by an absorbing layer is an oversimplified view compared to the simulations described in Section 4.2, which take into account a realistic volume emission rate, mixed with hydrocarbons which absorb the emission in several layers along the line of sight. Unfortunately, the energy determination relies on a modeled vertical distribution of hydrocarbons which was not validated by observational results in high latitude regions. Gérard et al. (2009) determined that the maximum of the H_2 ultraviolet auroral emission in the midnight sector was, on the average, located in the 800–1200 km region. Within the Monte Carlo simulations described here, the 800 km level is reached for electrons with $E_0 = 1$ keV. Several possibilities may be put forward to reconcile the high altitude value derived from the limb images with the presence of CH_4 absorption in 6 of the 10 spectra described in Table 4. One is that the spectra analyzed in this work may not be typical and that Saturn's aurora generally does not show signature of methane absorption in agreement with the Voyager reports. It would also agree with Gustin et al.'s (2009) conclusion that auroral emission originates from regions near the homopause level. A second explanation is that the analysis of auroral limb images was entirely based on altitude determination above the nightside limb, whereas all except one of the present spectra were collected on the dayside. It is possible that, on average the electron energy is harder in the dayside sector and lowers the altitude of the aurora near or slightly below the methane homopause. A third possible explanation would be that the atmosphere is non-hydrostatic in the presence of upwelling, pushing the CH_4 homopause up to about 1000 km. Finally, the most plausible, is related to the thermal structure of the auroral upper atmosphere. Gérard et al. (2009) and Gustin et al. (2009) suggested that the model atmosphere by Moses et al. (2000) adapted to high latitudes was not appropriate for use at auroral altitudes. Gérard et al. (2009) raised the possibility that the auroral thermospheric temperature rapidly increases in the 100 to 1 bar region, in contrast to the gradient observed during the low-latitude Voyager occultation measurements. If so, the altitude of the methane homopause is likely lower than at low or mid-latitudes. In this case, the pressure-altitude relationship and the methane altitude distribution in the vicinity of the homopause used in our determination of the electron energy may be subject to revision when models or observations appropriate to high altitudes become available.

6. Conclusions

Some of the STIS and UVIS spectra of Saturn's main auroral oval obtained during the coordinated HST-Cassini spectral campaign in March and April 2011 show signatures of moderate absorption by methane, although other spectra are not absorbed at short FUV wavelengths. Our analysis indicates that the slant CH_4 column overlying the auroral layer is quite variable, ranging from less than 5×10^{15} to 2×10^{16} cm^{-2}. These results confirm earlier findings

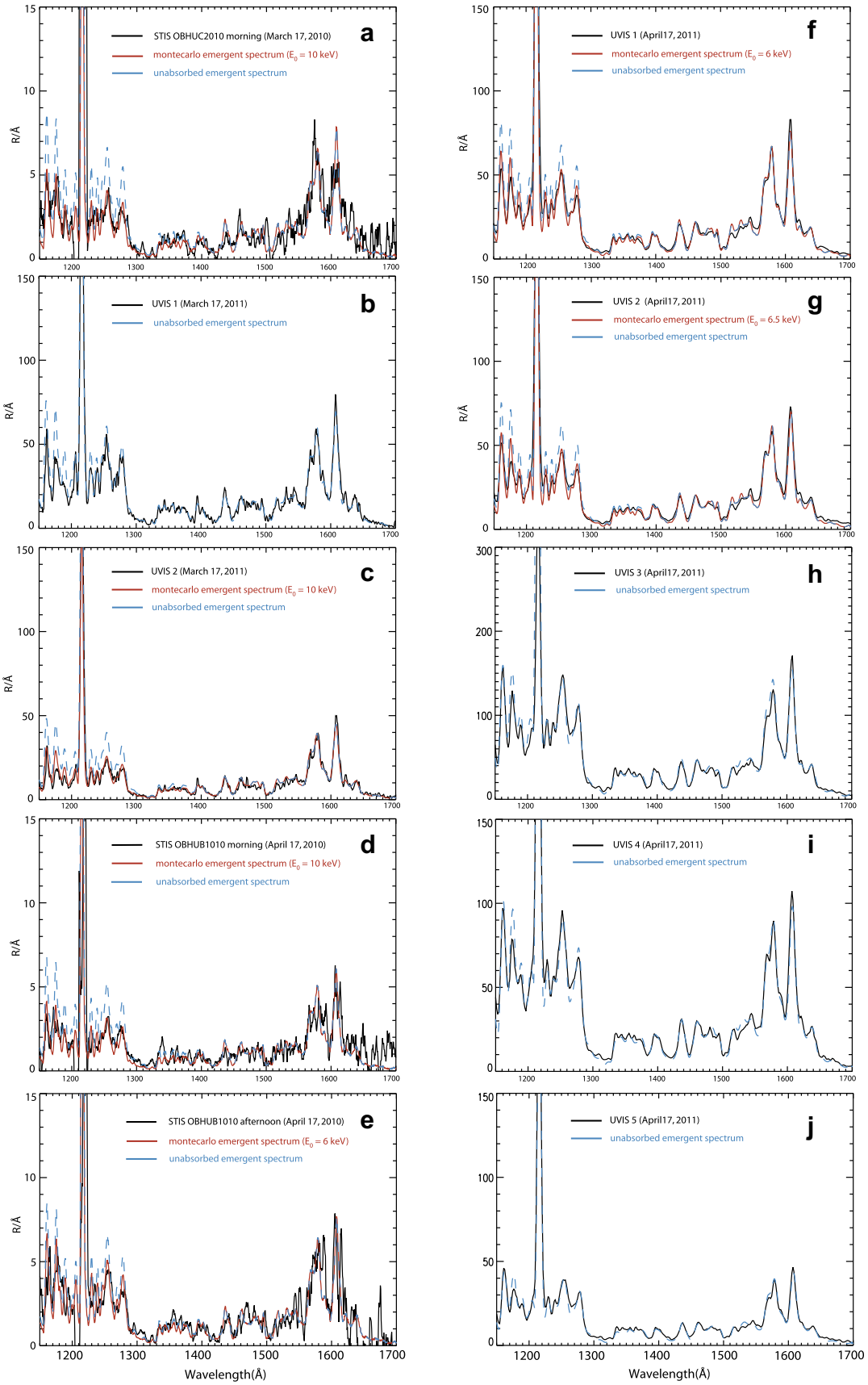

Fig. 4. Auroral spectra obtained on March 17 and April 17, 2011. In each one, the black solid line represents the observations, the blue dotted line the unabsorbed laboratory spectrum and the red solid line the laboratory spectrum calculated with the multi-layer model, as described by formulae (1) and (2).

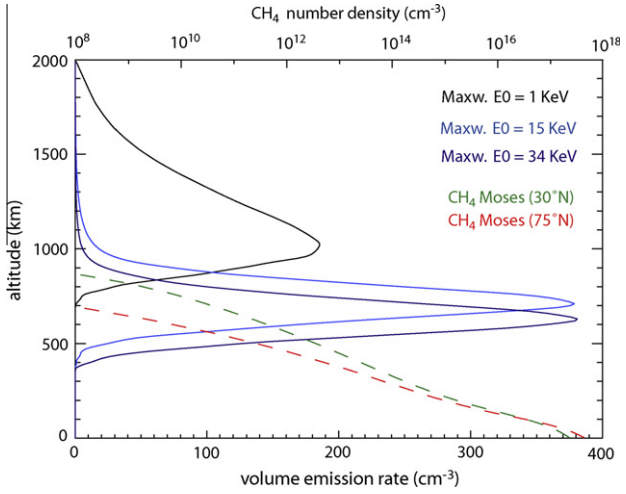

Fig. 5. Vertical distribution of the volume emission rate of the total emission rate of the H_2 Lyman and Werner bands (lower axis). These profiles were calculated for Maxwellian energy distributions of the precipitated electron flux characterized by E_0 = 1, 10 and 15 keV using a Monte Carlo direct simulation method. The dotted lines show the distribution of the methane number density (upper axis) in the original Moses et al. (2000) model at 30° (in green) and in the version corrected for the high-latitude gravity value (in red).

from Voyager UVS, HST-STIS and Cassini-UVIS indicating that absorption by methane is either absent or moderate in Saturn's aurora. The only model atmosphere currently available is based on low-latitude occultation measurements. Further observations and modeling of the high-latitude thermosphere of Saturn are clearly needed to better quantify the thermal structure and composition of the high-latitude upper atmosphere of Saturn.

Based on the methane vertical distribution in this model adapted to polar latitudes and on a Monte Carlo code simulating the auroral emission from electron precipitation, we derive mean electron energies ($2E_0$) ranging from less than 3 keV up to about ~20 keV, which sets the altitude of the auroral peak sometimes as low as 640 km. Such low altitude values are consistent with previous determinations obtained from auroral spectra, but different from the range 800 to 1200 km based on the altitude of the emission layer observed on FUV HST images of the nightside auroral limb. These differences suggest that different auroral structures probably correspond to different characteristic energies, a situation frequently observed in the Earth's aurora.

Acknowledgments

J.C.G., D.G. and A.R. acknowledge support from the Belgian Fund for Scientific Research (FNRS). Partial funding for this research was provided by the PRODEX program of the European Space Agency, managed in collaboration with the Belgian Federal Science Policy Office. Work in Boston and Central Arizona College was supported by grant HST-GO-12235.01 from the Space Telescope Science Institute to Boston University. W. Pryor acknowledges support from the Cassini Project and the University of Colorado for this work.

This work is based on observations with the NASA/ESA Hubble Space Telescope, obtained at the Space Telescope Science Institute, which is operated by AURA for NASA.

References

Badman, S.V. et al., 2011. Cassini VIMS observations of latitudinal and hemispheric variations in Saturn's infrared auroral intensity. Icarus 216, 367–375.

Badman, S.V. et al., 2012. Cassini observations of ion and electron beams at Saturn and their relationship to infrared auroral arcs. J. Geophys. Res. 117, A01211. http://dx.doi.org/10.1029/2011JA017222.

Bonfond, B., Grodent, D., Gérard, J.-C., Radioti, A., Dols, V., Delamere, P.A., Clarke, J.T., 2009. The Io UV footprint: Location, inter-spot distances and tail vertical extent. J. Geophys. Res. 114, A07224. http://dx.doi.org/10.1029/2009JA014312.

Broadfoot, A.L. et al., 1981. Extreme ultraviolet observations from Voyager 1 encounter with Saturn. Science 212, 206–211.

Bunce, E.J. et al., 2008. Origin of Saturn's aurora: Simultaneous observations by Cassini and the Hubble Space Telescope. J. Geophys. Res. 113, A09209.

Clarke, J.T., Moos, H.W., Atreya, S.K., Lane, A.L., 1981. IUE detection of bursts of H LY α emission from Saturn. Nature 290, 226–227. http://dx.doi.org/10.1038/290226a0.

Clarke, J.T. et al., 2009. Response of Jupiter's and Saturn's auroral activity to the solar wind. J. Geophys. Res. 114, A05210. http://dx.doi.org/10.1029/2008JA013694.

Cowley, S.W.H. et al., 2008. Auroral current systems in Saturn's magnetosphere: Comparison of theoretical models with Cassini and HST observations. Ann. Geophys. 26, 2613–2630.

Dalgarno, A., Yan, M., Liu, W., 1999. Electron energy deposition in a gas mixture of atomic and molecular hydrogen and helium. Astrophys. J. Suppl. Ser. 125, 237–256.

Dziczek, D., Ajello, J.M., James, G.K., Hansen, D.L., 2000. Cascade contribution to the H_2 Lyman band system from electron impact. Phys. Rev. A 61, 64702-1–64702-4.

Esposito, L.W. et al., 2004. The Cassini ultraviolet imaging spectrograph investigation. Space Sci. Rev. 115, 299–361.

Garvey, R.H., Green, A.E.S., 1976. Energy-apportionment techniques based upon detailed atomic cross sections. Phys. Rev. A 14, 946–953.

Garvey, R.H., Porter, H.S., Green, A.E.S., 1977. An analytic degradation spectrum for H_2. J. Appl. Phys. 48, 190–193.

Geballe, T.R., Jagod, M.-F., Oka, T., 1993. Detection of H_3^+ infrared emission lines in Saturn. Astrophys. J. Lett. 408, L109–L112.

Gérard, J.-C., Dols, V., Grodent, D., Waite, J.H., Gladstone, G.R., Prangé, R., 1995. Simultaneous observations of the Saturnian aurora and polar haze with the HST/FOC. Geophys. Res. Lett. 22, 2685–2688.

Gérard, J.-C., Grodent, D., Gustin, J., Saglam, A., Clarke, J.T., Trauger, J.T., 2004. Characteristics of Saturn's FUV aurora observed with the Space Telescope Imaging Spectrograph. J. Geophys. Res. 109, A09207. http://dx.doi.org/10.1029/2004JA010513.

Gérard, J.-C., Bunce, E.J., Grodent, D., Crowley, S.W.H., Clarke, J.T., Badman, S.V., 2005. Signature of Saturn's auroral cusp: Simultaneous Hubble Space Telescope FUV observations and upstream solar wind monitoring. J. Geophys. Res. 110, A11201. http://dx.doi.org/10.1029/2005JA011094.

Gérard, J.-C. et al., 2009. Altitude of Saturn's aurora and its implications for the characteristic energy of precipitated electrons. Geophys. Res. Lett. 36, L02202. http://dx.doi.org/10.1029/2008GL036554.

Grodent, D., Gérard, J.-C., Cowley, S.W.H., Bunce, E.J., Clarke, J.T., 2005. The global morphology of Saturn's southern ultraviolet aurora. J. Geophys. Res. 110, A01207. http://dx.doi.org/10.1029/2004JA010717.

Grodent, D., Gustin, J., Gérard, J.-C., Radioti, A., Bonfond, B., Pryor, W.R., 2011. Small scale structures in Saturn's ultraviolet aurora. J. Geophys. Res. 116, A09225. http://dx.doi.org/10.1029/2011JA016818.

Gustin, J., Feldman, P.D., Gérard, J.-C., Grodent, D., Vidal-Madjar, A., Ben Jaffel, L., Desert, J.-M., Moos, H.W., Sahnow, D.J., Weaver, H.A., Wolven, B.C., Ajello, J.M., Waite, J.H., Roueff, E., Abgrall, H., 2004. Jovian auroral spectroscopy with FUSE: Analysis of self-absorption and implications for electron precipitation. Icarus 171, 336–355.

Gustin, J., Gérard, J.-C., Pryor, W., Feldman, P.D., Grodent, D., Holsclaw, G., 2009. Characteristics of Saturn's polar atmosphere and auroral electrons derived from HST/STIS, FUSE and Cassini/UVIS spectra. Icarus 200, 176–187.

Gustin, J., Bonfond, B., Grodent, D., Gérard, J.-C., 2012. Conversion from HST ACS and STIS auroral counts into brightness, precipitated power, and radiated power for H_2 giant planets. J. Geophys. Res. 117, A07316. http://dx.doi.org/10.1029/2012JA017607.

Jackman, C.H., Garvey, R.H., Green, A.E.S., 1977. Electron impact on atmospheric gases: I. Updated cross sections. J. Geophys. Res. 82, 5081–5090.

Kameta, K., Kouchi, N., Ukai, M., Hatano, Y., 2002. Photoabsorption, photoionization, and neutral-dissociation crosssections of simple hydrocarbons in the vacuum ultraviolet range. J. Elec. Spect. Rel. Phen. 123, 225–238.

Kimble, R.A. et al., 1998. The on-orbit performance of the Space Telescope Imaging Spectrograph. Astrophys. J. 492, L83. http://dx.doi.org/10.1086/311102.

Kurth, W.S. et al., 2009. Auroral processes. In: Dougherty, M.K., Esposito, L.W., Krimigis, S.M. (Eds.), Saturn from Cassini-Huygens. Springer.

Lee, A.Y.T., Yung, Y.L., Cheng, B.M., Bahou, M., Chung, C.-Y., Lee, Y.P., 2001. Enhancement of deuterated ethane on Jupiter. Astrophys. J. 551, L93–L96.

McGrath, M.A., Clarke, J.T., 1992. H I Lyman alpha emission from Saturn (1980–1990). J. Geophys. Res. 103 (20), 237.

Melin, H., Miller, S., Stallard, T., Trafton, L.M., Geballe, T.R., 2007. Variability in the $H3^+$ emission of Saturn: Consequences for ionisation rates and temperature. Icarus 186, 234–241.

Moses, J.I., Bézard, B., Lellouch, E., Feuchtgruber, H., Gladstone, G.R., Allen, M., 2000. Photochemistry of Saturn's atmosphere. I. Hydrocarbon chemistry and comparisons with ISO observations. Icarus 143, 244–298.

Müller-Wodarg, I.C.F., Mendillo, M., Yelle, R.V., Aylward, A.D., 2006. A global circulation model of Saturn's thermosphere. Icarus 180, 147–160.

Nichols et al., 2010. Variation of Saturn's UV aurora with SKR phase. J. Geophys. Res. 37, L15102. http://dx.doi.org/10.1029/2010GL044057.

Radioti, A. et al., 2011. Bifurcations of the main auroral ring at Saturn: Ionospheric signatures of consecutive reconnection events at the magnetopause. J. Geophys. Res. 116, A11209. http://dx.doi.org/10.1029/2011JA016661.

Sandel, B.R., Broadfoot, A.L., 1981. Morphology of Saturn's aurora. Nature 292, 679–682.

Sandel, B.R., Shemansky, D.E., Broadfoot, A.L., Holberg, J.B., Smith, G.R., 1982. Extreme ultraviolet observations from the Voyager 2 encounter with Saturn. Science 215, 548–553.

Shemansky, D.E., Ajello, J.M., 1983. The Saturn spectrum in the EUV: Electron excited hydrogen. J. Geophys. Res. 88, 459–464.

Shematovich, V.I., Bisikalo, D.V., Gérard, J.C., 1994. A kinetic model of the formation of the hot oxygen geocorona: 1. Quiet geomagnetic conditions. J. Geophys. Res. 99, 23217–23228.

Shyn, T.W., Sharp, W.E., 1981. Angular distributions of electrons elastically scattered from H_2. Phys. Rev. A 24, 1734–1740.

Smith, C.G.A., Aylward, A.D., Millward, G.H., Miller, S., Moore, S.L.E., 2007. An unexpected cooling effect in Saturn's upper atmosphere. Nature 445, 399–401.

Stallard, T., Miller, S., Melin, H., Lystrup, M., Dougherty, M.K., Achilleos, N., 2007. Saturn's auroral/polar H_3^+ infrared emission I. General morphology and ion velocity structure. Icarus 189, 1–13.

Stallard, T.S., Melin, H., Miller, S., Badman, S.V., Brown, R.H., Baines, K.H., 2012. Peak emission altitude of Saturn's H_3^+ aurora. Geophys. Res. Lett. 39, L15103. http://dx.doi.org/10.1029/2012GL052806.

Talboys et al., 2011. Statistical characteristics of field-aligned currents in Saturn's nightside magnetosphere. J. Geophys. Res. 116, A04213.

Trauger, J.T. et al., 1998. Saturn's hydrogen aurora: Wide field and planetary camera 2 imaging from the Hubble Space Telescope. J. Geophys. Res. 103 (20), 237.